photonics

MDPI

Article

A Tunable Hydrogen-Bond-Mediated Polymer-Based Mechanical Approach for Non-Destructive Cleaning of Silver Films

Yuhang Zhang [1,2], Yun Du [1,2], Tao Shen [1], Xingyue Gao [1], Kaipeng Liu [1,2], Yunfei Luo [1,2], Chengwei Zhao [1,2], Zeyu Zhao [1,2], Changtao Wang [1,2] and Ling Liu [1,2,*]

[1] State Key Laboratory of Optical Field Manipulation Science and Technologies, Institute of Optics and Electronics, Chinese Academy of Sciences, Chengdu 610209, China
[2] School of Optoelectronics, University of Chinese Academy of Sciences, Beijing 100049, China
* Correspondence: lling09@126.com

Abstract

Silver films are key building blocks for plasmonic and nanophotonic devices, whose optical performance and device reliability are highly sensitive to particulate contamination introduced during fabrication and operation. Herein, a non-destructive surface cleaning strategy specifically applicable to silver film systems is proposed, based on the synergistic regulation of the mechanical properties of a polymer layer and its interfacial adhesion to the silver film. Such regulation is achieved by tuning hydrogen-bond-mediated interactions within a modified poly(vinyl alcohol) (PVA) layer, enabling effective control over the locus of fracture during peeling, such that fracture preferentially occurs at the polymer/silver interface. Unlike conventional polymer-assisted cleaning methods that suffer from an inherent trade-off between bulk cohesion and interfacial adhesion, this approach decouples the two properties through molecular-level hydrogen-bond redistribution. As a result, particulate contaminants can be efficiently removed from the silver surface while preserving the structural integrity of the silver film. The proposed method achieves a particle removal efficiency of up to 98% for contaminants larger than 30 nm and can be stably applied to silver films with lateral dimensions ranging from 1 inch to 12 inches, demonstrating excellent scalability. By further adjusting the processing parameters and compositional ratios of the polymer layer, this strategy is expected to be adaptable to silver films with different thicknesses and structural configurations, providing a reliable surface cleaning solution for improving the performance and reliability of plasmonic and optoelectronic thin-film devices.

Keywords: silver films; plasmonic thin films; surface conditioning; interface engineering; polymer–metal adhesion; particulate contamination removal; optoelectronic device reliability

Received: 11 February 2026
Revised: 27 March 2026
Accepted: 4 April 2026
Published: 8 April 2026

1. Introduction

With the rapid advancement of thin-film fabrication technologies, silver thin films, owing to their excellent electrical conductivity, mechanical flexibility, and high optical transparency, have become indispensable functional layers in a wide range of next-generation optoelectronic devices [1]. As a result, silver films have demonstrated broad application prospects in fields such as flexible electronics [2,3], display technologies [4–6], and photovoltaic devices [7,8]. Moreover, by engineering multilayer architectures composed of alternating silver and dielectric layers, silver films can exhibit pronounced surface plasmon

resonance effects, enabling advanced photonic functionalities. Such plasmonic structures have been widely employed in optoelectronic detection [9], surface-enhanced Raman scattering [10], and other emerging nanophotonic applications.

Despite these advantages, silver films are highly susceptible to surface contamination during fabrication, transfer, and device integration processes. In particular, the adsorption of nano- and microscale particulate contaminants on the film surface can severely degrade their electrical and optical performance, compromise mechanical integrity, and induce device-level failures such as current leakage and micro-masking effects, ultimately reducing device yield and reliability. For example, in organic light-emitting diode (OLED) electrodes, Li_2O particles with diameters of 0.03–0.05 μm on silver films have been reported to induce current leakage densities of approximately 0.1 $A \cdot m^{-2}$ under an applied voltage of 30 V [11].

Therefore, effective cleaning strategies are crucial for maintaining the performance and stability of silver films. Conventional cleaning techniques can generally be categorized into chemical and physical approaches. Chemical methods, such as acidic or alkaline solutions, tend to corrode silver films and degrade pattern resolution [12,13], whereas physical cleaning methods, including laser cleaning and supercritical cleaning, often cause irreversible mechanical damage to fragile thin films [14]. Although hybrid chemical–physical cleaning strategies have been developed to mitigate these issues [15–17], they still suffer from inherent limitations, including limited cleanable areas, poor adaptability to complex substrate geometries, and insufficient protection of delicate nanostructures.

Polymer sacrificial layer-based cleaning strategies offer a viable pathway to overcoming these limitations. In such approaches, a polymer layer is spin-coated to encapsulate particulate contaminants and subsequently remove them, thereby avoiding direct damage to the silver film during the cleaning process. The cleaning performance of these methods largely depends on the removal behavior of the polymer layer. However, in the absence of interfacial and mechanical regulation of the polymer removal process, existing polymer removal strategies, including vacuum-assisted delamination [18], mechanical peeling [19], and chemical dissolution [20], often suffer from critical drawbacks, such as limited processable areas, uncontrollable stresses during removal that lead to silver film damage, or residual chemical contaminants after polymer removal. Consequently, achieving a balance among large-area processability, high particle removal efficiency, and non-destructive treatment of the substrate remains a major challenge.

To address this challenge, we propose a non-destructive cleaning strategy for silver films based on the regulation of the mechanical properties of a polymer layer. By precisely tuning the overall mechanical properties of a modified poly(vinyl alcohol) (PVA) layer and its interfacial adhesion to the silver film, the originally uncontrollable mechanical peeling process can be transformed into a well-controlled interfacial fracture behavior. Specifically, the fracture interface is designed to preferentially occur at the polymer/silver interface rather than within the polymer layer or the silver film. Through molecular-level hydrogen-bond redistribution, this design decouples bulk cohesion from interfacial adhesion—a capability that is intrinsically limited in conventional polymer-based cleaning methods. This controlled mechanical peeling enables the intact removal of the solid polymer layer together with encapsulated particulate contaminants while preserving the structural integrity of the silver film. Under optimized conditions, the proposed method achieves a particle removal efficiency of up to 98% for contaminants larger than 30 nm and is applicable to silver films with lateral dimensions ranging from 1 inch to 12 inches and diverse structural configurations. This strategy provides a scalable and general surface treatment pathway for the high-quality cleaning of plasmonic silver films and other metallic thin films, offering significant potential for improving the performance and reliability of optoelectronic and nanophotonic devices.

2. Materials and Methods

This section describes the materials, experimental procedures, and simulation methods employed for the polymer-assisted cleaning of silver films. The preparation of polymer solutions, polymer-assisted cleaning procedures, and characterization techniques are detailed to ensure experimental reproducibility. In addition, the evaluation of particle removal efficiency and molecular dynamics simulations are presented to support a comprehensive investigation of the cleaning process.

2.1. Materials and Polymer Solution Preparation

Poly(vinyl alcohol) (PVA, degree of hydrolysis ≈ 88%) was purchased from Macklin (Shanghai, China) and used as the primary polymer matrix without further purification. A carbonyl-containing hydrogen-bond-accepting polymer additive, which belongs to the general chemical class of water-soluble polymers bearing tertiary amide groups, was introduced as an auxiliary component to regulate the hydrogen-bonding network within the PVA matrix. This class of non-ionic polymers possesses bulky side groups and provides strong hydrogen-bond acceptors without acting as donors. All polymer solutions were prepared using deionized water as the solvent.

An aqueous PVA solution with a final concentration of 18 wt% was prepared by dissolving PVA in deionized water under continuous stirring at 300 rpm. The dissolution process was conducted at 90 °C for approximately 4 h to ensure complete dissolution and the formation of a homogeneous solution. After the PVA solution was fully prepared, the hydrogen-bond-accepting polymer additive was added to the solution at a final concentration of 0.6 wt% with respect to the total solution. The resulting PVA/additive mixed solution was subsequently stirred at room temperature without additional heating until a uniform and stable solution was obtained.

2.2. Polymer-Assisted Cleaning Procedure

Silver films were used as the target substrates for the cleaning experiments. The prepared PVA or PVA/additive polymer solutions were deposited onto the surface of the silver films by spin coating at a rotation speed of 1000 rpm (resulting in a polymer film thickness of approximately 2.67 μm) with an acceleration of 250 rpm·s^{-1}, forming a uniform polymer layer that encapsulated surface particulate contaminants (Figure 1). After deposition, the samples coated with the polymer layer were thermally cured at 80 °C for 15 min to promote solvent evaporation and stabilize the polymer layer. Following curing, the edge of the polymer film was gently lifted using tweezers, and the polymer layer was then manually peeled off at a slow and approximately constant speed. All peeling tests were performed by the same operator using a constant peeling angle (~15° relative to the film surface) and a slow, steady speed to ensure reproducibility. This peeling process enabled the simultaneous mechanical removal of the polymer layer together with the embedded particulate contaminants while maintaining the structural integrity of the underlying silver film.

2.3. Characterization Methods

The surface morphology and cleanliness of the silver films before and after cleaning were characterized using optical microscopy (OM), charge-coupled device (CCD) imaging, and scanning electron microscopy (SEM). OM and CCD imaging were employed for large-area inspection and particle distribution analysis, while SEM was used to resolve nanoscale surface features and residual particulate contaminants. In addition, cross-sectional transmission electron microscopy (TEM) was performed to examine the thickness, uniformity, and structural integrity of the silver layers before and after cleaning.

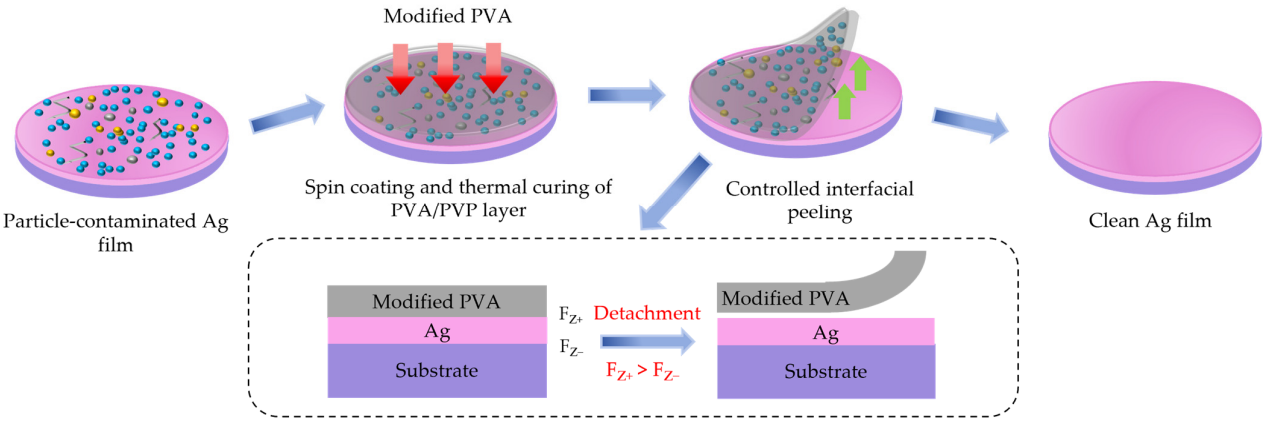

Figure 1. Schematic of the polymer-assisted cleaning process for Ag films, illustrating polymer coating, thermal curing, and controlled interfacial peeling. The blue arrows indicate the sequence of the process flow and direct to the cross-sectional mechanism, while the red and green arrows represent the direction of polymer application and the peeling force, respectively.

Atomic force microscopy (AFM) was utilized to evaluate surface morphology and to quantify changes in surface roughness induced by the cleaning process. AFM measurements with different scan sizes were conducted to analyze nanoscale topographical features. White light interferometry (WLI) was further employed to characterize surface roughness over large lateral areas, providing complementary multiscale surface information.

Fourier transform infrared spectroscopy (FTIR) was used to investigate chemical interactions and hydrogen-bonding behavior within the polymer layers. X-ray photoelectron spectroscopy (XPS) was performed to analyze the chemical states and bonding environments at the polymer/silver interface.

Nanoscratch testing was conducted to evaluate the mechanical response and interfacial adhesion of the polymer layers, thereby probing their resistance to mechanical deformation and interfacial fracture behavior. Thermogravimetric analysis combined with differential scanning calorimetry (TG–DSC) was used to assess the thermal stability and thermal transition behavior of the polymer systems.

2.4. Evaluation of Particle Removal Efficiency

The particle removal efficiency was quantitatively evaluated using an automated surface defect inspection system, which enables full-wafer particle mapping and statistical analysis over entire 8-inch wafers. To eliminate edge-handling artifacts, a standard edge exclusion zone (indicated by the red boundary in the mapping results, typically 3 mm) was applied, and particles within this zone were excluded from counting. Surface defect maps were acquired for silver films before and after the cleaning process to determine the spatial distribution and size of particulate contaminants.

Particle quantification was strictly performed using an automated counting algorithm rather than manual inspection. The detection threshold was calibrated using standard polystyrene latex (PSL)-equivalent spheres. Specifically, the system was configured to capture and count particles with a diameter of >30 nm based on laser light scattering intensity. All particle statistics were automatically identified and quantified by the inspection system based on these predefined thresholding parameters. The particle removal efficiency (η) was calculated according to the following equation:

$$\eta = \frac{N_0 - N_1}{N_0} \times 100\% \quad (1)$$

where N_0 and N_1 represent the total particle counts measured before and after cleaning, respectively.

2.5. Molecular Dynamics Simulations

Molecular dynamics (MD) simulations were conducted using the Materials Studio software (v2020) package (BIOVIA, Dassault Systèmes). Poly(vinyl alcohol) (PVA) chains and model polymer chains representing a carbonyl-containing hydrogen-bond-accepting additive were constructed using the Polymer module, with degrees of polymerization of 50 and 20, respectively. Partial negative charges were assigned to the hydroxyl oxygen atoms of PVA and the carbonyl oxygen atoms of the hydrogen-bond-accepting additive to represent their hydrogen-bonding capability.

Amorphous PVA/additive blend systems with seven different compositions were generated using the Amorphous Cell module under periodic boundary conditions. All simulations were performed using the Forcite module. Hydrogen bonds were identified based on geometric criteria, with a donor–acceptor distance shorter than 2.5 Å and a D–H$\cdots$A angle larger than 90°. The evolution of hydrogen-bond populations and chain configurations was analyzed to elucidate the effect of hydrogen-bond-accepting additive incorporation on the hydrogen-bond network.

2.6. Thermodynamic Calculations and Surface Energy Analysis

To establish the theoretical removal threshold and evaluate the initial adhesion state of the contaminants, the van der Waals adhesion energy (E_{adh}) between the SiO_2 particle and the underlying Ag film was estimated based on the classic sphere-plane interaction model:

$$E_{adh} \approx -\frac{A_H R}{6z} \tag{2}$$

where R is the particle radius (15 nm) and z represents the standard physical adsorption equilibrium cut-off distance, typically taken as 0.4 nm for such solid–solid contacts. The composite Hamaker constant (A_H) represents the interaction between the SiO_2 particle (phase 1) and the Ag substrate (phase 2) across the air medium (phase 3). Based on the macroscopic Lifshitz theory, A_H was calculated using the individual Hamaker constants in vacuum for SiO_2 ($A_{11} = 6.5 \times 10^{-20}$ J) [21] and Ag ($A_{22} = 4.0 \times 10^{-19}$ J) [22], yielding a value of approximately 1.61×10^{-19} J.

Subsequently, to quantitatively evaluate the thermodynamic driving force for particle removal during the peeling process, the surface energy components of the polymer films were determined using the Owens-Wendt-Rabel-Kaelble (OWRK) approach. Contact angles of two standard test liquids with known surface tension components—deionized water (highly polar) and diiodomethane (highly dispersive)—were measured on the polymer surfaces. The solid–solid interfacial energy ($\gamma_{p/pol}$) between the contaminant particle (p) and the polymer film (pol) was calculated as:

$$\gamma_{p/pol} = \gamma_p + \gamma_{pol} - 2\sqrt{\gamma_p^d \gamma_{pol}^d} - 2\sqrt{\gamma_p^p \gamma_{pol}^p} \tag{3}$$

where the superscripts d and p denote the dispersive and polar components, respectively. The surface energy parameters for the highly hydrophilic SiO_2 standard particle ($\gamma_p = 76.65$ mJ/m^2, $\gamma_p^d = 43.00$ mJ/m^2, $\gamma_p^p = 33.65$ mJ/m^2) were adopted from established literature [23]. For the final absolute energy gain ($|E_{gain}|$) calculations, the effective exposed surface area (SA) of the 30 nm particle was approximated using an idealized spherical geometry ($SA = 4\pi R^2$).

3. Results and Discussion

3.1. Polymer System Screening and Interfacial Interaction Mechanism

3.1.1. Screening of Conventional Peelable Polymer Systems

To evaluate the feasibility of using peelable polymer layers for particulate removal from silver films, several commonly employed polymer systems, including poly(methyl methacrylate) (PMMA), poly(dimethylsiloxane) (PDMS), and hyaluronic acid (HA), were first investigated. However, all three materials exhibited pronounced limitations when applied to this cleaning scenario.

PMMA showed strong interfacial interactions with the silver film. During peeling, ethanol-assisted ultrasonication was required to detach the PMMA layer, which resulted in extensive cracking and fragmentation of the underlying silver film (Figure 2a). In addition, PMMA requires thermal curing at approximately 150 °C, a temperature range that induces significant oxidation of the silver film, as evidenced by the Ag XPS spectra (Figure 2b). This thermal incompatibility further compromises the interfacial integrity of the metal layer.

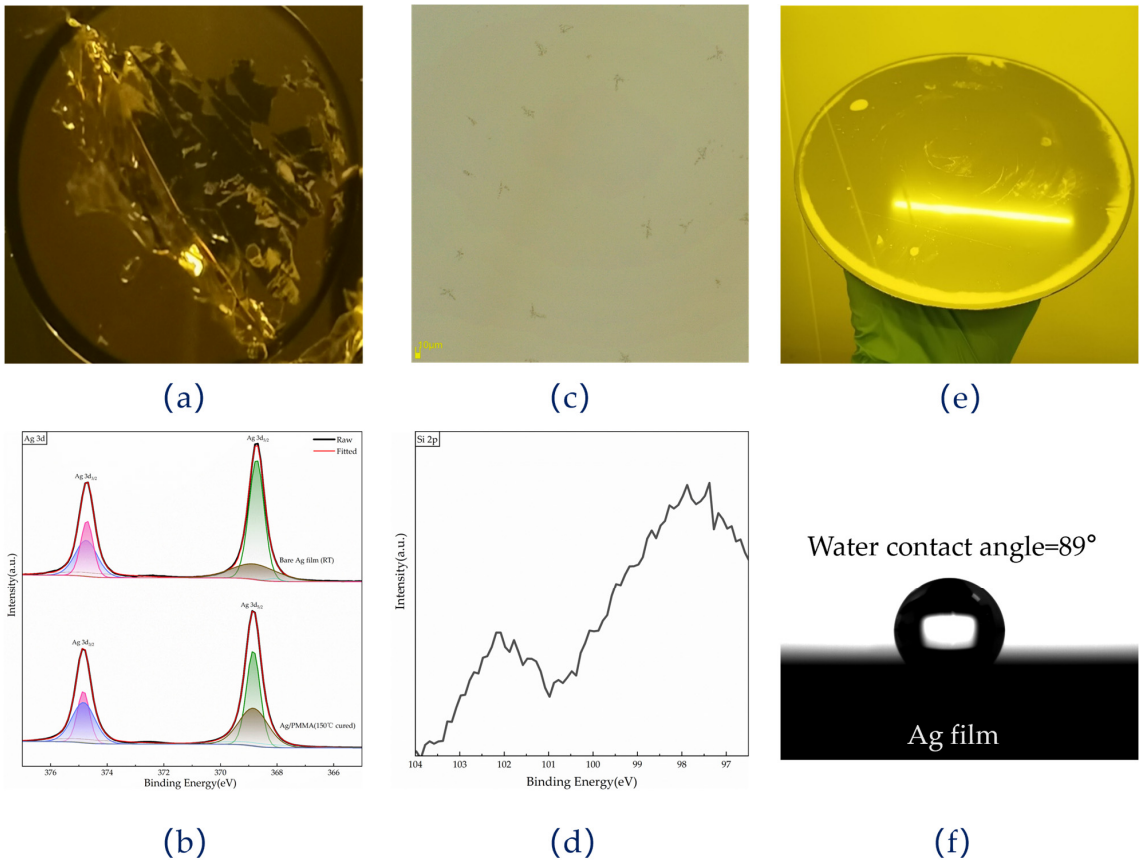

Figure 2. Failure modes of representative polymer systems during polymer-assisted cleaning of silver films. (**a**) Optical image showing severe cracking and fragmentation of the silver film after peeling of the PMMA layer assisted by ethanol ultrasonication; (**b**) Ag 3d XPS spectra of silver films before and after PMMA curing at 150 °C, indicating pronounced oxidation induced by high-temperature processing, where the green and pink shaded regions represent metallic silver (Ag), while the brown and blue regions indicate oxidized silver species; (**c**) Optical microscopy image revealing polymer residue on the silver surface after peeling of the PDMS layer due to cohesive failure within the polymer; (**d**) High-resolution XPS spectrum in the Si 2p region collected from the silver surface after PDMS removal, confirming the presence of silicon-containing residues; (**e**) Optical image showing film rupture and damage to the underlying silver layer caused by poor film continuity of the hyaluronic acid (HA) layer during peeling; (**f**) Water contact angle measurement of the bare silver film (≈89°), indicating moderate hydrophobicity that hinders uniform wetting and film formation of the highly hydrophilic HA solution.

In contrast, PDMS exhibited insufficient bulk cohesive strength. During peeling, cohesive failure preferentially occurred within the PDMS layer, leading to polymer residue remaining on the silver surface (Figure 2c). High-resolution XPS analysis in the Si 2p region revealed a pronounced silicon signal on the silver surface after peeling (Figure 2d), confirming the presence of silicon-containing residues consistent with PDMS. These results demonstrate that, due to unavoidable cohesive fracture and polymer transfer during peeling, PDMS cannot achieve clean interfacial separation.

HA displayed a distinct failure mode associated with poor film formation. Water contact angle measurements indicate that the bare silver film exhibits moderate hydrophobicity, with a contact angle of approximately 89° (Figure 2f), which inhibits uniform wetting and spreading of the highly hydrophilic HA solution. As a result, HA failed to form a continuous polymer film with sufficient mechanical integrity on the silver surface. The poor film continuity and inadequate cohesive strength led to film rupture during peeling, accompanied by damage to the underlying silver layer (Figure 2e).

Taken together, these polymer systems exhibit intrinsic, structure-related limitations. The high polarity and high-temperature curing requirement of PMMA hinder simultaneous control of interfacial adhesion and silver film stability; the chemically inert backbone and low surface energy of PDMS promote cohesive failure and polymer residue; and the strong hydrophilicity of HA leads to poor film continuity and interfacial mismatch on moderately hydrophobic silver surfaces. Consequently, none of these materials can provide a viable processing window through simple adjustment of composition or processing parameters.

It is worth noting that thermal exposure above approximately 100 °C induces surface roughening and oxidation of silver films, resulting in a pronounced decrease in optical reflectivity and increased scattering [24], which is highly detrimental to their application as reflective electrodes in optoelectronic devices. Based on these observations, an ideal polymer layer for non-destructive particulate removal from silver films should satisfy three fundamental criteria:

(i) tunable interfacial adhesion strength, stronger than particle–silver interactions but weaker than the cohesive strength of the polymer layer;
(ii) low-temperature processability (<100 °C) to avoid silver oxidation;
(iii) the ability to form flexible, continuous, residue-free films with sufficient cohesive strength.

3.1.2. Interfacial Hydrogen-Bonding Interaction Between PVA Layers and Ag Films

Compared with PMMA, PDMS, and HA, poly(vinyl alcohol) (PVA) provides a uniquely tunable and process-compatible polymer system for peelable cleaning of silver films. PVA films can be formed under mild thermal conditions (e.g., curing at approximately 60 °C [25]), which is sufficient for solvent removal and physical network stabilization without inducing thermally driven oxidation or degradation of the silver film. In addition, the hydroxyl-rich molecular structure of PVA enables moderate and adjustable interfacial interactions, making it particularly suitable for non-destructive peeling. Based on these considerations, PVA was selected as the polymer layer material in this study.

To elucidate the interfacial interaction mechanism between PVA and silver films, high-resolution X-ray photoelectron spectroscopy (XPS) and Fourier transform infrared spectroscopy (FTIR) were employed. Figure 3a compares the O 1s spectra of PVA films supported on silicon and silver substrates. For PVA on silicon, the O 1s spectrum is dominated by a high-binding-energy component associated with free hydroxyl groups. In contrast, when PVA is deposited onto the silver substrate by spin coating, the spectral weight shifts markedly toward lower binding energies, accompanied by the emergence of a distinct hydrogen-bonded –OH component. Quantitative deconvolution reveals that

this hydrogen-bonded –OH component accounts for approximately 45.8% of the total O 1s peak area, whereas the free –OH component constitutes 54.2%. Specifically, these interfacial hydrogen bonds are formed between the hydrogen atoms of the PVA hydroxyl groups and the oxygen atoms on the naturally oxidized silver surface. The binding energy difference between the free –OH and hydrogen-bonded –OH components is approximately 0.9 eV, reflecting a moderate change in the local electronic environment induced by hydrogen-bond formation between PVA hydroxyl groups and the naturally oxidized silver surface. Importantly, no spectral features characteristic of Ag–O–C covalent bond formation were observed within the detection limits of XPS, suggesting the absence of irreversible chemical anchoring at the interface.

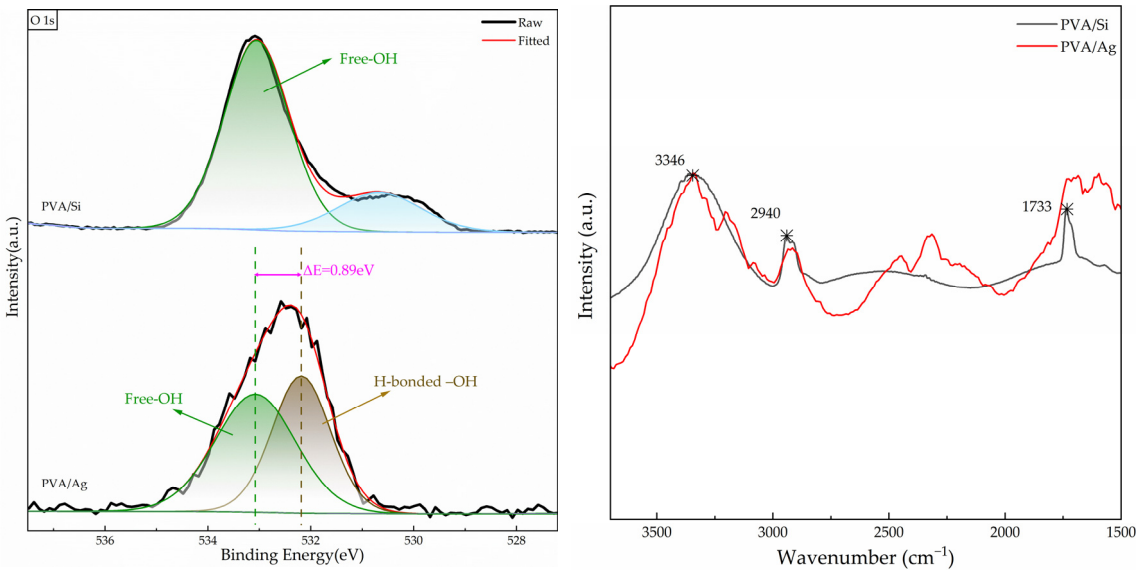

Figure 3. Spectroscopic characterization of interfacial interactions between poly(vinyl alcohol) (PVA) and silver films. (**a**) High-resolution O 1s XPS spectra of PVA films supported on silicon (PVA/Si) and silver (PVA/Ag) substrates, showing a redistribution of spectral weight toward lower binding energies and the emergence of a hydrogen-bonded –OH component for PVA/Ag ($\Delta E \approx 0.9$ eV); (**b**) FTIR spectra of PVA films on silicon and silver substrates, where the O–H stretching band (~3346 cm^{-1}) exhibits a red shift of ~5–6 cm^{-1} upon contact with silver. In (**a**), the green and brown shaded areas correspond to the free –OH and hydrogen-bonded –OH components, respectively.

FTIR analysis further supports the hydrogen-bond-dominated interaction. As shown in Figure 3b, the O–H stretching vibration of PVA supported on silicon appears at approximately 3346 cm^{-1}, characteristic of weakly associated hydroxyl groups. Upon contact with the silver surface, this band exhibits a red shift of approximately 5–6 cm^{-1}, consistent with the formation of interfacial hydrogen bonds of moderate strength. Such a limited red shift is a typical signature of non-covalent hydrogen bonding, in contrast to the much larger spectral changes generally associated with strong chemical bonding.

A key advantage of this hydrogen-bond-mediated interaction lies in its tunability, which provides a flexible means to modulate interfacial adhesion at the polymer–silver interface. Hydrogen bonding between the PVA layer and the silver film affords sufficient adhesion to stabilize the polymer layer during coating and low-temperature curing, while avoiding irreversible chemical anchoring. Meanwhile, the internal hydrogen-bond network within the PVA matrix offers a versatile handle for tailoring the cohesive properties of the polymer layer through polymer composition and processing conditions. Compared with PMMA, PDMS, and HA, this hydrogen-bond-enabled tunability endows PVA with

a broader and more accessible processing window, forming the basis for controllable, low-damage peelable cleaning of silver films.

3.1.3. Energy-Based Consideration for Peelable Particle Removal

The successful removal of particulate contaminants from silver film surfaces depends on the competition between particle–substrate adhesion and the energy released during polymer peeling. For nano- and microscale particles, adhesion to metal surfaces is predominantly governed by van der Waals interactions. Accordingly, the particle–silver film adhesion energy can be approximately calculated using Equation (2), where A_H denotes the Hamaker constant of the particle–silver film system, R is the particle radius, and z represents the equilibrium separation distance. Owing to the high polarizability of silver, the Hamaker constant of such systems is relatively large [26], resulting in strong particle adhesion. Consequently, the direct removal of particles from silver film surfaces is intrinsically challenging.

It should be noted that Equation (2) represents an idealized scenario. In practical environments, the actual adhesion is more complex, depending on factors such as contact geometry (e.g., surface roughness) and potential capillary forces. Nevertheless, this simplified model provides a physical baseline for quantifying the relevant energy scale. To establish this baseline, SiO_2 is selected as a representative model for typical process contaminants. For a 30 nm SiO_2 particle (the lower detection limit of our characterization, R = 15 nm), the composite Hamaker constant A is approximately 1.61 $\times$ 10^{-19} J based on Lifshitz theory. Consequently, the theoretical van der Waals adhesion energy is estimated to be on the order of 1.01 $\times$ 10^{-18} J. Removing smaller particles is thermodynamically more demanding, as the peeling energy gain scales with the particle's effective surface area (R^2), whereas the adhesion energy scales only linearly with the radius (R). Therefore, satisfying the energetic criterion for 30 nm particles ensures the effective removal of larger contaminants.

During the peeling process, particle transfer from the silver surface to the polymer layer is energetically favorable only when the absolute interfacial energy gain ($|E_{gain}|$) arising from polymer delamination and polymer–particle interactions exceeds the magnitude of the particle–silver film adhesion energy ($|E_{adh}|$), i.e.,

$$|E_{gain}| \geq |E_{adh}| \tag{4}$$

In the present PVA-based system, the moderate and tunable hydrogen-bond-mediated interactions at the PVA–silver interface provide sufficient interfacial adhesion to enable effective stress transfer during peeling. At the same time, the relatively high bulk cohesive strength of the PVA film suppresses cohesive failure within the polymer layer. As a result, the energetic criterion for particle transfer is satisfied, allowing particulate contaminants to be removed together with the polymer layer without leaving residues on the underlying silver film or inducing mechanical or chemical damage. This energy-based analysis provides a mechanistic explanation for the experimentally observed large-area, residue-free peeling behavior.

3.2. Decoupling Cohesion and Interfacial Adhesion in PVA-Based Systems

3.2.1. Intrinsic Limitations of Neat PVA Systems

To achieve damage-free removal of particulate contaminants from silver films, the polymer layer must simultaneously exhibit sufficient bulk cohesion to maintain film integrity during peeling and sufficiently low interfacial adhesion to enable clean separation from the Ag surface. We first examined whether this balance could be achieved by tuning the intrinsic material parameters of neat PVA.

Increasing the degree of hydrolysis, molecular weight, or solution solid content enhances intermolecular hydrogen bonding and chain entanglement within the PVA matrix, resulting in mechanically robust and continuous films. However, these same parameters inevitably increase the density of hydroxyl groups at the interface, leading to excessively strong hydrogen-bond-mediated adhesion to the native oxide on the Ag surface. As a consequence, peeling of such films often induces partial delamination or mechanical damage of the Ag layer.

Conversely, reducing the hydroxyl content, molecular weight, or solid content effectively weakens polymer–Ag interfacial adhesion but simultaneously compromises the bulk cohesion of the PVA film. Under these conditions, the polymer layer tends to undergo cohesive failure during peeling, leaving polymer residues on the Ag surface and preventing effective particulate removal.

Representative peeling results obtained from PVA films spanning different degrees of polymerization, hydrolysis, and solid content consistently reveal this trade-off (Figure 4). These observations demonstrate that, in neat PVA systems, bulk cohesion and interfacial adhesion are intrinsically coupled through the same hydrogen-bonding interactions. As a result, no accessible processing window exists in which both requirements can be satisfied through simple parameter tuning, highlighting the fundamental limitation of neat PVA for Ag film cleaning.

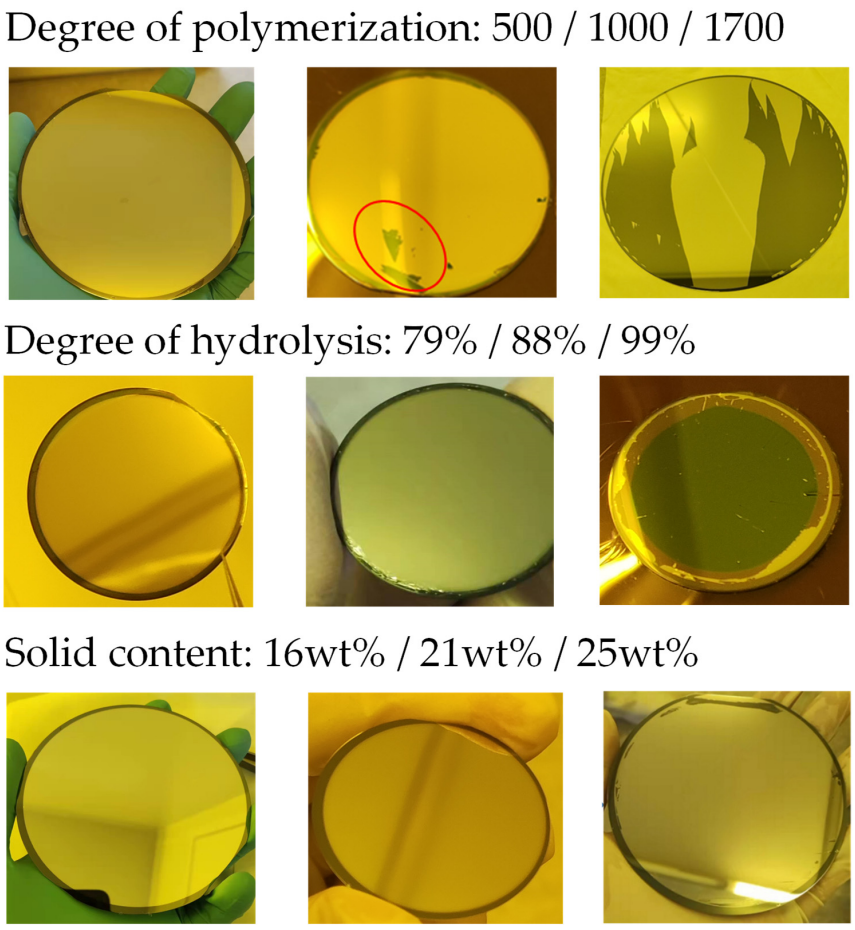

Figure 4. Representative peeling results of neat PVA films deposited on ultrathin Ag films under different intrinsic material parameters, including degree of polymerization, degree of hydrolysis, and solution solid content. Variations in these parameters lead to either excessive interfacial adhesion with partial Ag film damage or insufficient bulk cohesion accompanied by cohesive failure and polymer residues, indicating a trade-off between interfacial adhesion and bulk cohesion in neat PVA systems. The circled regions highlight areas of partial Ag film damage.

3.2.2. Additive-Induced Hydrogen-Bond Redistribution for Decoupling Cohesion and Interfacial Adhesion

To overcome the intrinsic limitation of neat PVA systems, in which enhancement of bulk cohesion is typically accompanied by a concurrent increase in polymer–silver interfacial adhesion, a carbonyl-containing hydrogen-bond-accepting polymer additive was introduced to reconstruct the internal hydrogen-bonding network of the polymer at the molecular level. As schematically illustrated in Figure 5, PVA chains are originally interconnected through intramolecular and intermolecular hydrogen bonds involving hydroxyl (–OH) groups. Upon incorporation of the hydrogen-bond-accepting additive, the carbonyl (C=O) groups act as strong hydrogen-bond acceptors and form tunable intermolecular hydrogen bonds with PVA hydroxyl groups, without introducing covalent crosslinking.

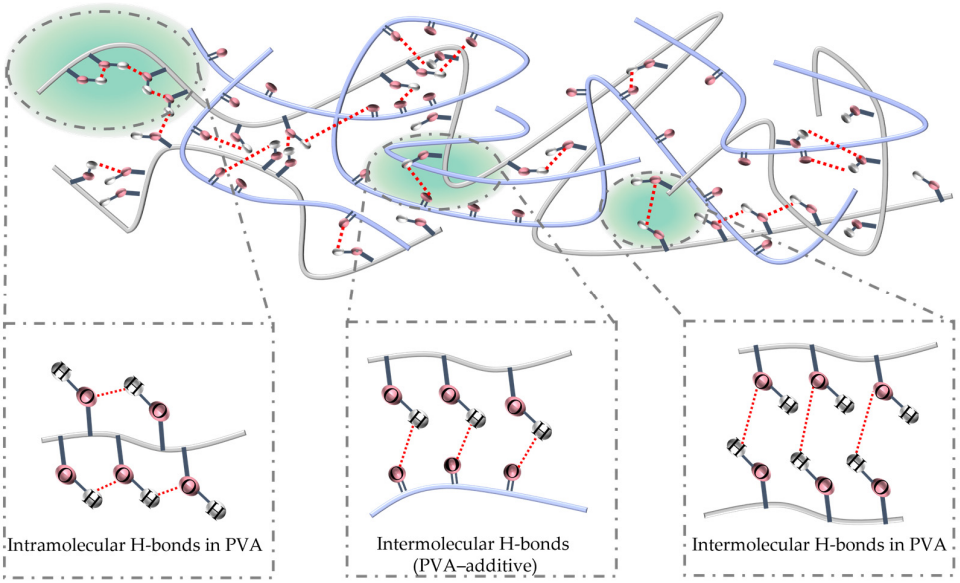

Figure 5. Schematic illustration of hydrogen-bond network reconstruction in the modified PVA system. In neat PVA, polymer chains are connected through intra- and intermolecular hydrogen bonds among hydroxyl groups. Upon incorporation of a carbonyl-containing hydrogen-bond-accepting additive, intermolecular hydrogen bonding is established between PVA hydroxyl groups and carbonyl groups of the additive, leading to a redistribution of hydrogen bonding within the polymer network. In the schematic, the gray and blue tubes represent the PVA and additive backbones. The red/white and standalone red spheres denote hydroxyl groups and carbonyl oxygen, respectively, with red dashed lines indicating hydrogen bonds.

This hydrogen-bond redistribution, as depicted in Figure 5, partially redirects hydrogen-bonding interactions from the polymer–silver interface to the polymer interior. This shift increases the density of physical crosslinks within the matrix and reduces the free PVA hydroxyl sites available to bond with the native silver oxide layer. Consequently, the bulk cohesive strength of the polymer layer is enhanced, whereas the effective interfacial adhesion to the silver film is moderated. This molecular-level reconstruction of the hydrogen-bond network provides a mechanistic basis for mitigating the intrinsic coupling between cohesion and adhesion in neat PVA systems, thereby enabling the formation of mechanically robust, continuous peelable films while maintaining sufficiently weak interfacial adhesion for damage-free delamination of ultrathin silver films.

Molecular dynamics simulations provide a direct visualization of how the incorporation of a hydrogen-bond-accepting additive reconstructs the polymer network structure under both equilibrated and stretched states. As shown in Figure 6, increasing the additive fraction alters chain packing and connectivity within the modified PVA network.

At moderate additive contents, the network maintains a more continuous load-bearing structure during stretching, whereas excessive additive incorporation leads to pronounced local aggregation and structural heterogeneity, resulting in discontinuous network deformation under tensile strain. These results indicate that additive incorporation not only enhances the cohesive characteristics of the polymer matrix but also optimizes the network topology through composition-dependent hydrogen-bond organization, thereby improving structural integrity during deformation processes relevant to polymer peeling.

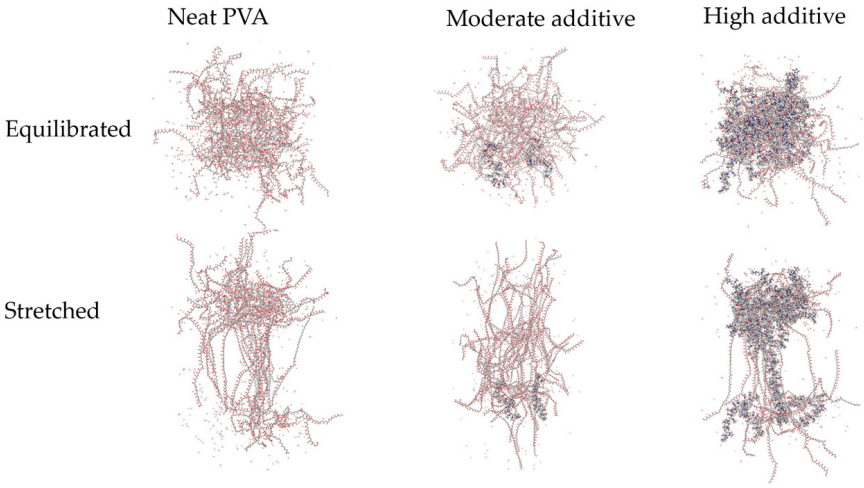

Figure 6. Representative molecular dynamics configurations of the modified PVA network at different additive contents under equilibrated (**top row**) and stretched (**bottom row**) states. From left to right: neat PVA, moderate additive content, and high additive content. Moderate additive content yields a more continuous, load-bearing network during stretching, whereas excessive additive incorporation induces localized aggregation and structural heterogeneity. In the molecular representations, the gray, white, red, and blue spheres denote carbon, hydrogen, oxygen, and nitrogen atoms, respectively.

From a quantitative perspective, the simulated hydrogen-bond statistics exhibit a non-monotonic dependence on additive content. As shown in Figure 7a, the total number of hydrogen bonds remains high at low additive contents, whereas excessive additive incorporation leads to a pronounced decrease in the overall hydrogen-bond population. This non-monotonic trend originates from the specific structural characteristics of the carbonyl-containing polymer. At a low additive content, its carbonyl groups function as strong acceptors to establish effective interactions with PVA. However, as the additive concentration increases, the lack of hydrogen-bond donors in this polymer decreases the density of effective hydrogen-bonding sites within the system. Meanwhile, the pronounced steric hindrance generated by its bulky side groups expands the spatial distance between PVA segments, thereby disrupting the inherently dense network and causing a significant decline in the number of intramolecular hydrogen bonds. Consequently, moderate additive incorporation promotes effective hydrogen-bond connectivity, while excessive additive disrupts the homogeneity of the hydrogen-bond network.

Consistent with this structural evolution, the simulated stress–strain responses in Figure 7b reveal that compositions with moderate additive content exhibit enhanced load-bearing capability and improved deformation stability compared with neat PVA, whereas higher additive contents result in reduced mechanical robustness. Together, these results suggest that moderate additive incorporation enables efficient load transfer while preventing severe network disruption during deformation.

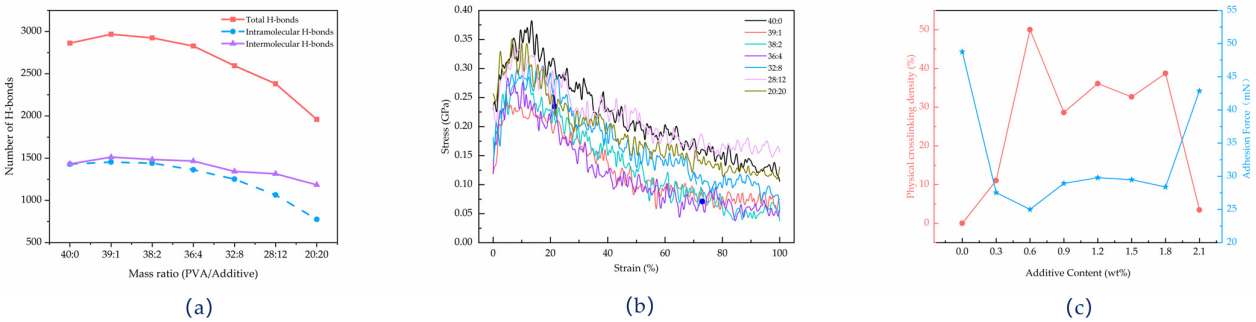

Figure 7. Characterization of the PVA/additive systems with varying additive content: (**a**) The number of total, intramolecular, and intermolecular hydrogen bonds as a function of the mass ratio of PVA to the additive; (**b**) Stress–strain curves for the different PVA/additive compositions under mechanical stretching; (**c**) Physical crosslinking density (red) and interfacial adhesion force (blue) as a function of additive content, showing the influence of the additive on the polymer network and adhesion.

At the macroscopic level, this mechanism manifests as an opposite evolution of bulk cohesion and interfacial adhesion with increasing additive content. As shown in Figure 7c, the physical crosslink density (red curve) increases sharply and reaches a maximum at an additive content of 0.6 wt%, followed by a decrease at higher additive concentrations, indicating that this optimal composition most effectively enhances bulk cohesion. In contrast, the interfacial adhesion force (blue curve) exhibits the opposite trend, reaching a pronounced minimum at the same additive loading.

This anticorrelated behavior constitutes the key innovation of the present design. By redistributing hydrogen bonds from the polymer–silver interface to the polymer bulk, additive incorporation enables simultaneous enhancement of bulk cohesion and attenuation of interfacial adhesion. In conventional reinforcement strategies, increased cohesion is typically accompanied by stronger interfacial adhesion, thereby reducing peelability. In contrast, the coincident extrema observed at 0.6 wt% additive—namely, a maximum in physical crosslink density and a minimum in interfacial adhesion—directly demonstrate that a single-component-controlled polymer system can concurrently satisfy the conflicting requirements of cohesion enhancement and adhesion reduction.

Spectroscopic and relaxation measurements further corroborate the enhancement of internal hydrogen-bonding interactions upon additive incorporation. As shown in Figure 8a, the O–H stretching vibration shifts from approximately 3340 cm^{-1} in neat PVA to around 3246 cm^{-1} in the PVA/additive system, corresponding to a red shift of ~94 cm^{-1}, which is indicative of significantly strengthened hydrogen bonding. Meanwhile, the emergence and intensification of carbonyl-related bands (e.g., near 1680 cm^{-1}) confirm the participation of the additive in the intermolecular hydrogen-bond network.

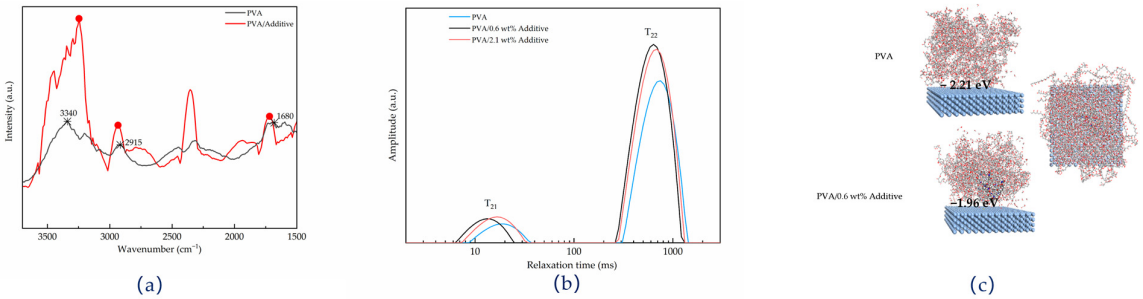

Figure 8. (**a**) FTIR spectra, (**b**) T_2 relaxation behavior, and (**c**) simulated polymer–Ag interfacial structures of neat PVA and PVA/additive systems, revealing enhanced internal hydrogen bonding and weakened polymer–Ag interactions after additive incorporation.

Complementary low-field nuclear magnetic resonance (NMR) T_2 relaxation measurements (Figure 8b) reveal composition-dependent constraints on molecular dynamics. The systematic evolution of characteristic relaxation signals indicates increased physical crosslink density and reduced mobility of polymer chains and associated water molecules at the optimal composition, supporting the formation of a denser and more strongly connected bulk network facilitated by additive incorporation.

At the polymer–silver interface, simulation results further quantify the anticipated weakening effect. As shown in Figure 8c, the calculated adsorption energy decreases from 2.21 eV for neat PVA to 1.96 eV for the PVA/0.6 wt% additive system, corresponding to a reduction of approximately 11.3%. This decrease is consistent with the proposed hydrogen-bond redistribution mechanism, in which the population of free hydroxyl groups available for hydrogen bonding with the native silver oxide is reduced, thereby lowering interfacial coupling strength and facilitating clean peeling.

Overall, the incorporation of the additive provides a controllable noncovalent interaction pathway that simultaneously enhances bulk cohesion—by increasing the physical crosslink density—and reduces interfacial adhesion—by lowering the polymer–silver adsorption energy and minimizing interfacial bonding sites. The identification of an optimal additive content of approximately 0.6 wt% establishes a practical material design guideline for peelable cleaning applications. At this composition, the polymer film attains sufficient mechanical robustness to enable intact peeling while maintaining sufficiently low interfacial adhesion to avoid damage to the silver layer, thereby offering a stable processing window for residue-free and low-damage particulate removal.

3.2.3. Quantitative Validation of the Energy-Based Removal Criterion

To quantitatively validate the strategy established in Section 3.1.3, the actual energy gain ($|E_{gain}|$) during the peeling process was evaluated. Based on static contact angle measurements (Figure 9) and the Owens-Wendt-Rabel-Kaelble (OWRK) approach, the absolute interfacial energy gain for particle encapsulation can be expressed as:

$$\left|E_{gain}\right| = (\gamma_p + \gamma_{pol} - \gamma_{p/pol}) \times SA \quad (5)$$

where γ_p, γ_{pol} and $\gamma_{p/pol}$ represent the surface energy of the particle, the surface energy of the polymer film, and the solid–solid interfacial energy between the particle and the polymer, respectively. SA denotes the effective exposed surface area of the particle. Consistent with our theoretical baseline, a 30 nm SiO_2 particle ($SA \approx 2.83 \times 10^{-15}$ m^2, with a highly hydrophilic γ_p of 76.65 mJ/m^2) was utilized as the standard contaminant model.

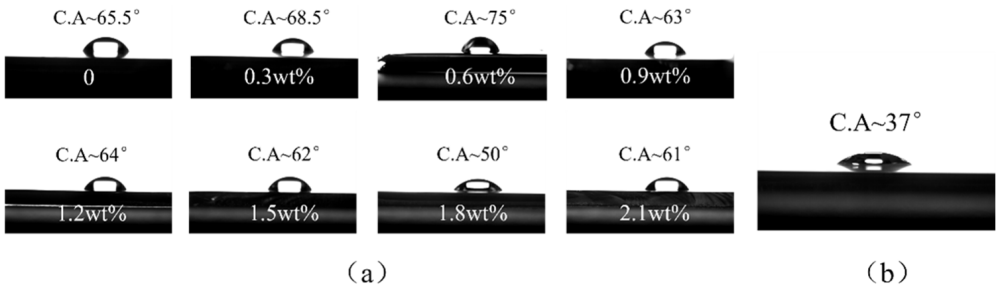

Figure 9. Static contact angles of the polymer films with varying additive contents: (**a**) water contact angles as a function of additive content; (**b**) a representative image of the diiodomethane contact angle (the values remained stable at ~37° across all samples).

As summarized in Table 1, the additive induces a molecular-level reconstruction of the hydrogen-bond network. This optimizes the polymer's total surface energy to 46.41 mJ/m^2 at a 0.6 wt% concentration. Calculations reveal that under this optimal formulation, the

energy gain ($|E_{gain}|$) for peeling the encapsulated particle is 3.11×10^{-16} J, which is over two orders of magnitude higher than the theoretical van der Waals adhesion threshold (1.01×10^{-18} J).

Table 1. Surface energy parameters of the polymer films and the corresponding absolute energy gain ($|E_{gain}|$) for removing a 30 nm SiO_2 particle.

Additive Content (wt%)	γ_{pol} (mJ/m^2)	$\gamma_{p/pol}$ (mJ/m^2)	$\|E_{gain}\|$ (10^{-16} J)
0	49.88	7.62	3.37
0.3	48.78	9.18	3.29
0.6 (Optimized)	46.41	12.96	3.11
0.9	51.14	6.56	3.43
1.2	50.95	7.09	3.42
1.5	51.65	6.17	3.45
1.8	58.86	2.71	3.75
2.1	52.49	5.89	3.48

This confirms a synergistic effect: while the hydrogen-bond redistribution intentionally weakens substrate adhesion to protect the silver film, the thermodynamic driving force remains exceptionally sufficient for thorough particle detachment, successfully overcoming the intrinsic limitations of neat PVA systems.

3.3. Process Regulation of Interfacial Adhesion

After confirming that the PVA/additive blend system enables a tunable balance between bulk cohesion and interfacial adhesion, process optimization was further employed to refine the interfacial interactions and identify a narrow yet practical processing window for damage-free peeling. Within this window, the interfacial adhesion must be sufficiently strong to ensure effective particle capture, while remaining low enough to allow clean delamination without damaging the silver layer. Curing temperature, curing time, and polymer film thickness were identified as three key process parameters governing this balance.

The curing temperature directly influences both the intrinsic stability of the silver surface and the polymer–silver interfacial interactions. Molecular dynamics simulations indicate that the surface energy of the Ag(110) facet increases monotonically with temperature (Figure 10a), suggesting enhanced surface activity at elevated temperatures. Correspondingly, as the temperature increases from 35 °C to 100 °C, the calculated polymer–silver interaction energy becomes progressively more negative (Figure 10b), implying a gradual strengthening of polymer–silver coupling under idealized conditions.

In contrast, experimentally measured adhesion force exhibits a non-monotonic dependence on curing temperature (Figure 10c). Moderate temperature elevation enhances adhesion, whereas excessive heating leads to a pronounced reduction in adhesion force. Specifically, curing at approximately 80 °C yields the highest and most stable adhesion response, while further temperature increase results in a clear decline. This discrepancy between simulation and experiment arises from additional factors present in real systems, including solvent evaporation kinetics, polymer chain rearrangement, and temperature-induced modification of the silver surface. Consequently, a relatively low curing temperature of ~80 °C represents an optimal compromise, providing sufficient interfacial interaction while avoiding excessive adhesion and silver surface degradation.

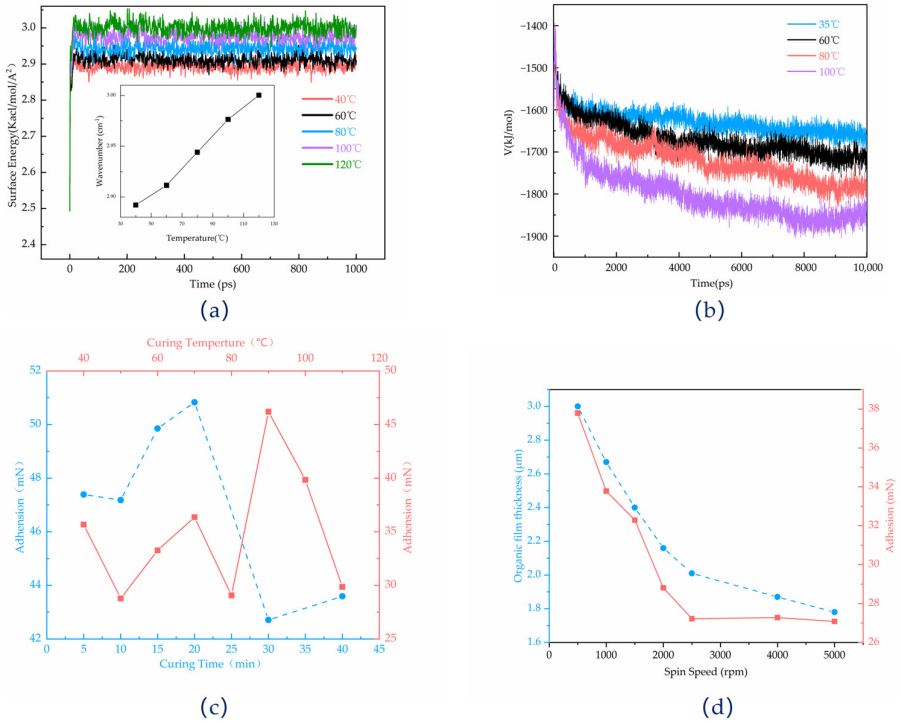

Figure 10. (**a**) Simulated surface energy evolution of the Ag(110) surface at different temperatures; (**b**) Simulated interaction energy between the PVA/additive blended film and the Ag surface as a function of temperature; (**c**) Experimentally measured adhesion force between the PVA/additive film and the Ag layer under different curing temperatures and curing times; (**d**) Dependence of the PVA/additive–Ag adhesion force on spin-coating speed, corresponding to different polymer film thicknesses.

The evolution of interfacial adhesion with curing time further reflects the non-equilibrium nature of interface formation. As shown in Figure 10c, at a fixed curing temperature, adhesion force initially increases and then decreases with curing time. During the early stage (approximately within the first 15–25 min), rapid solvent removal and polymer chain migration toward the interface promote hydrogen-bond formation, leading to a peak in adhesion force. Beyond this period, restricted chain mobility and the accumulation of internal stresses induce partial relaxation of interfacial interactions, causing the adhesion force to decrease and eventually stabilize. Based on this behavior, a curing time of 15 min was selected as optimal, ensuring sufficient interfacial bonding for particle capture while maintaining good peelability.

Polymer film thickness, controlled via spin-coating speed, also plays a critical role in interfacial adhesion (Figure 10d). Increasing the spin speed from 500 to 5000 rpm reduces the film thickness from approximately 3.0 μm to 1.8 μm, accompanied by a gradual decrease in adhesion force from ~38 mN to ~28 mN. Thicker films prepared at lower spin speeds provide larger interfacial contact areas and higher adhesion but are prone to cohesive failure due to stress accumulation during peeling. Conversely, excessively thin films formed at high spin speeds suffer from insufficient mechanical integrity, leading to tearing and incomplete removal. An intermediate spin speed of ~1000 rpm yields an optimal film thickness that balances adequate mechanical strength with moderate adhesion, enabling damage-free peeling.

Overall, quantitative regulation of curing temperature, curing time, and film thickness allows the interfacial adhesion of the PVA/additive–silver system to be precisely confined within a narrow damage-free peeling window. Combined with the molecular-level hydrogen-bond design described above, this process optimization establishes a coherent

strategy that links interfacial energetics, mechanical response, and practical processing, providing a comprehensive solution for efficient, residue-free cleaning of silver films.

From a throughput perspective, the entire cleaning cycle takes approximately 17 min. This is highly competitive with conventional wet chemical cleaning, which typically demands 20–30 min for sequential washing and stringent drying. Crucially, our dry peeling process completely eliminates the time-consuming post-cleaning drying bottleneck inherent to wet methods, thereby offering a highly efficient alternative to traditional solvent-based cleaning.

3.4. Performance Verification of the Optimized Cleaning Strategy

The performance of the optimized peelable polymer cleaning strategy was systematically evaluated using multiscale and multimodal characterization techniques, including optical microscopy (OM), CCD-based inspection, scanning electron microscopy (SEM), and particle statistical analysis. The top row in Figure 11 presents the surface state of the silver film prior to cleaning, while the bottom row shows the corresponding regions after cleaning.

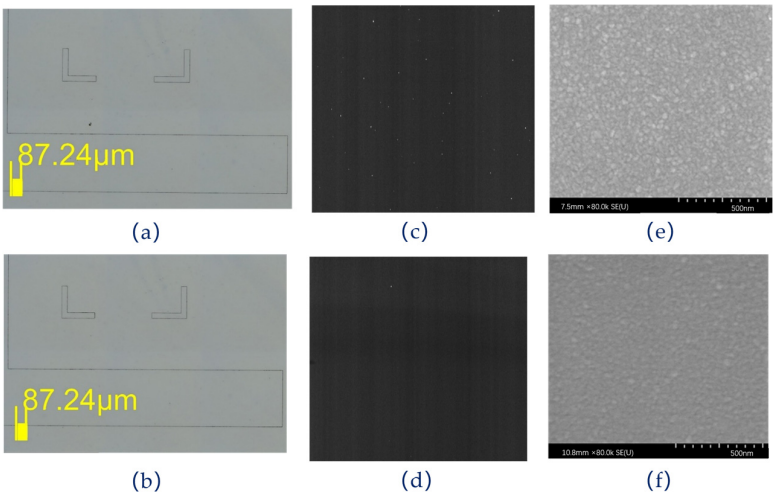

Figure 11. Multiscale characterization of the silver surface before and after cleaning using the optimized PVA/additive film: (**a**,**c**,**e**) Surface states before cleaning; (**b**,**d**,**f**) Surface states after cleaning. (**a**,**b**) OM images showing macroscopic surface integrity; (**c**,**d**) CCD inspection images revealing particle distribution; (**e**,**f**) SEM images detailing nanoscale morphology.

OM images (Figure 11a,b) indicate that the overall surface morphology of the silver film remains unchanged after cleaning, with no observable macroscopic defects or film damage. CCD inspection results (Figure 11c,d) reveal a large number of high-contrast particulate features on the silver surface before cleaning, whereas the surface becomes markedly more uniform after cleaning, with only a small number of isolated residual particles. SEM observations further confirm this trend at the nanoscale (Figure 11e,f), showing a pronounced reduction in particle density and a more homogeneous and smooth surface morphology following cleaning. The consistent results obtained from OM, CCD inspection, and SEM across different length scales collectively demonstrate that the proposed cleaning process efficiently removes surface particulate contaminants without introducing polymer agglomeration or residual contamination.

To quantitatively substantiate these morphological observations, full-wafer particle statistical analysis was performed. Considering that the baseline of native particulate contaminants naturally varies depending on specific micro/nanofabrication conditions, we evaluated the cleaning effectiveness across two distinct initial baselines to verify the method's robustness (Figure 12).

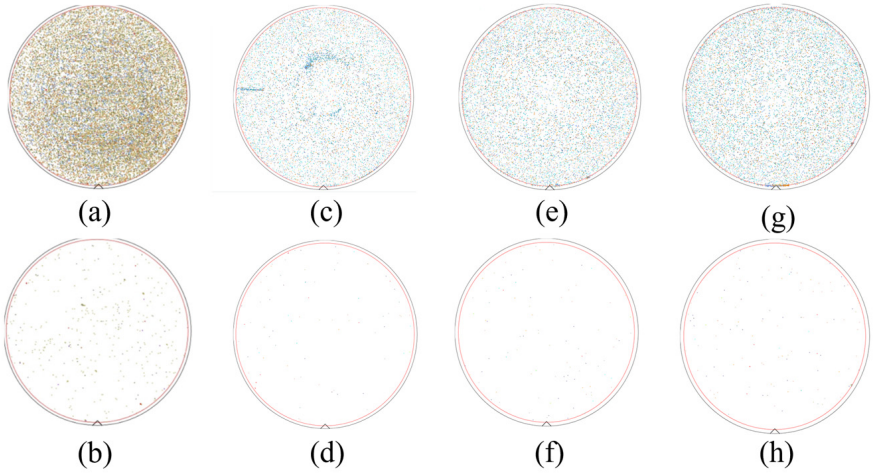

Figure 12. Full-wafer particle statistical analysis for the pristine and cleaned films across different initial contamination baselines. (**a**,**b**) Particle distribution maps of the pristine and cleaned films under a high initial contamination test scenario. (**c**–**h**) Particle distribution maps for three independent repeated experiments under a typical routine contamination baseline, showing states for the pristine (**c**,**e**,**g**) and cleaned (**d**,**f**,**h**) films. The repeated trials demonstrate an average removal efficiency of 99.21 ± 0.14%. In the particle distribution maps, the different colors of the dots represent various particle size ranges automatically assigned by the inspection tool. The denser visual appearance and distinct color distribution in subfigure (**a**) correspond to the significantly higher particle count (27,046) in the high-contamination scenario compared to the routine baselines in (**c**,**e**,**g**).

In a high initial contamination test scenario (Figure 12a,b), the initial particle count was 27,046. After our cleaning treatment, the count decreased to 493, corresponding to a removal efficiency of over 98% (calculation method detailed in Section 2). Furthermore, to evaluate the statistical reproducibility of the cleaning method, we performed three independent repeated experiments under a more typical routine contamination baseline (Figure 12c–h). In these trials, the initial particle counts were 13,219, 14,550, and 16,616, which drastically decreased to 92, 103, and 158 after cleaning, respectively. The results demonstrate that the average removal efficiency under this routine baseline reached 99.21%, with a minimal standard deviation of only 0.14%.

It should be noted that the inspection system used in this study has a detection limit of 30 nm, and the removal efficiency for particles below this size is not statistically evaluated here.

Cross-sectional transmission electron microscopy (TEM) provides direct structural evidence for the non-destructive nature of the polymer-assisted peeling process (Figure 13a,b). Specifically, by comparing the pristine Ag film (Figure 13a) with the cleaned Ag film (Figure 13b), both silver films maintain a continuous and dense layered structure in the central and edge regions, with a well-defined interface. At the current 20 nm observation scale, no cracks, local delamination, subsurface damage, or discernible modification of the original columnar grain morphology are observed. Based on statistical analysis of multiple cross-sectional measurements, the average thickness of the silver film changes only slightly from 12.55 nm for the pristine film to 12.52 nm for the cleaned film, corresponding to a variation of less than 0.3%. This consistency in both morphology and thickness across the entire layer demonstrates that the cleaning process does not introduce detectable mechanical damage, subsurface alteration, or material loss.

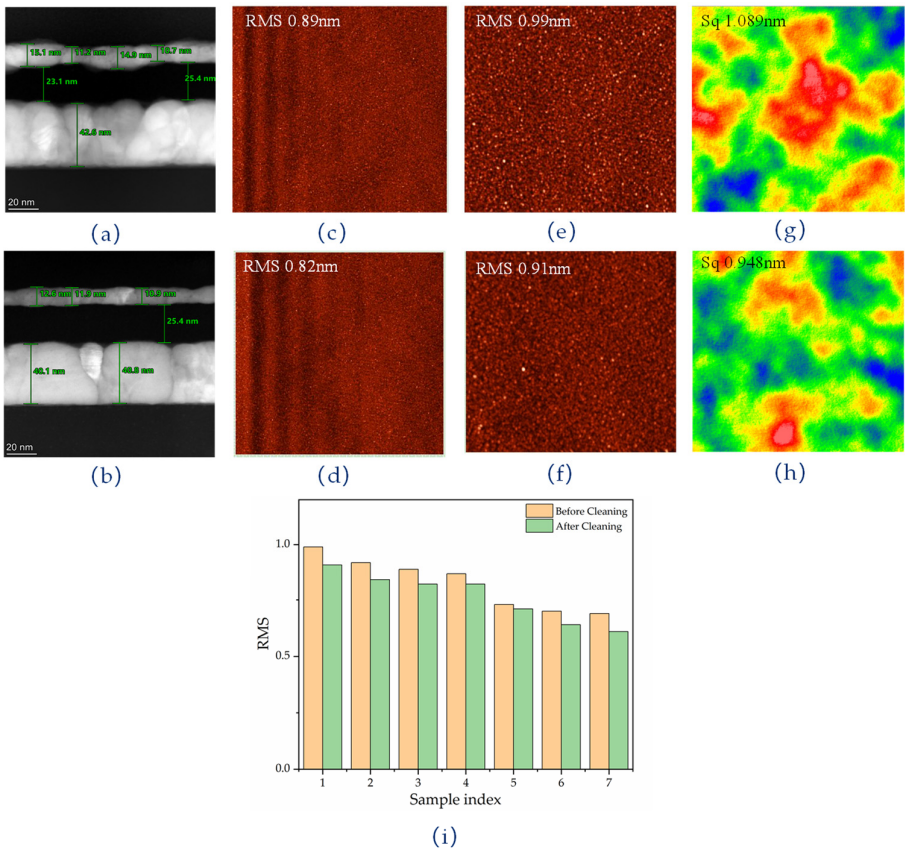

Figure 13. Characterization of silver film integrity and surface morphology of the pristine and cleaned films. (**a**,**b**) Cross-sectional TEM images showing the preserved layered structure and thickness consistency of the silver film; (**c**–**f**) AFM topographic images at scan sizes of 3 × 3 μm^2 (**c**,**d**) and 1 × 1 μm^2 (**e**,**f**), revealing reduced surface roughness for the cleaned films; (**g**,**h**) White-light interferometry images confirming macroscopic surface smoothing, where the color scale represents relative surface height, displaying a continuous gradient from the lowest valleys (blue) through intermediate heights (green, yellow, and orange) to the highest peaks (red); (**i**) Statistical comparison of RMS roughness values, demonstrating a consistent reduction in surface roughness across multiple samples.

Surface morphology analysis further confirms the mildness and stability of the cleaning strategy. Atomic force microscopy (AFM) measurements acquired over scan areas of 3 × 3 μm^2 show representative surface morphologies of the pristine Ag film (used as a control) and the cleaned Ag film in Figures 13c and 13d, respectively, while corresponding images at a smaller scan size of 1 × 1 μm^2 are presented in Figures 13e and 13f, respectively. At both scan scales, the root-mean-square (RMS) roughness of the cleaned Ag film is consistently lower than that of the pristine film. As summarized by the multi-point statistical results in Figure 13i, the average RMS roughness decreases by approximately 7.6%, indicating that the polymer peeling process inherently smooths the intrinsic surface undulations, resulting in an overall improvement in surface flatness. Large-area white-light interferometry measurements are consistent with the AFM observations (Figure 13g,h). A further reduction in RMS roughness is observed for the cleaned films, demonstrating that the intrinsic surface-smoothing effect is not limited to the local nanoscale but extends to the micrometer scale.

To evaluate the influence of the polymer-assisted cleaning process on the intrinsic functional properties of silver films, the optical response of the pristine and cleaned films was systematically analyzed. Ellipsometric data were fitted using the Cauchy model to extract the effective optical thickness and dielectric constants, with the corresponding results summarized in Table 2. The fitting results show that the effective optical thickness

changes slightly from 39.53 nm for the pristine film to 38.61 nm for the cleaned film, indicating a limited variation.

Table 2. Optical thickness parameter and dielectric constants extracted from Cauchy fitting for the pristine film and cleaned film.

Sample Condition	Thickness, *d* (nm) *	Real Part, ε_1	Imaginary Part, ε_2
Pristine film	39.51	−2.6549	0.2906
	39.50	−2.6559	0.3028
	39.60	−2.6546	0.3091
	39.53 (average)	−2.6551 (average)	0.3008 (average)
Cleaned film	38.58	−2.6488	0.3074
	38.53	−2.6497	0.3104
	38.73	−2.6417	0.3136
	38.61 (average)	−2.6467 (average)	0.3105 (average)

* *d* denotes the thickness parameter obtained from Cauchy model fitting of ellipsometric data (effective optical thickness) and is not directly comparable to the physical Ag thickness measured by cross-sectional TEM.

Meanwhile, the average real part of the dielectric constant (ε_1) exhibits a minor change from −2.6551 to −2.6467, corresponding to a small reduction in its absolute value, whereas the average imaginary part (ε_2) increases slightly from 0.3008 to 0.3105. Statistical analysis via an independent two-sample *t*-test reveals that these subtle shifts are not statistically significant ($p = 0.065$ for ε_1; $p = 0.121$ for ε_2) and fall entirely within the intrinsic measurement uncertainty (e.g., standard deviation of 0.0094 for pristine ε_2). This confirms that the cleaning process does not introduce substantial optical loss, effectively preserving the film's intrinsic optical properties. Crucially, high-performance plasmonic devices require both a stable intrinsic optical response and minimal surface scattering [27]. Therefore, these preserved dielectric parameters, combined with the observed 7.6% reduction in surface roughness (Figure 13i), strongly suggest that the fundamental plasmonic properties of the silver films are well-maintained, highlighting their potential for demanding optoelectronic applications.

At the macroscopic scale, the optimized cleaning strategy also demonstrates good stability and applicability. As shown in Figure 14, silver films with lateral dimensions ranging from 1 to 12 inches maintain their structural integrity during the peel-off cleaning process, enabling continuous, crack-free peeling over the entire film area (Figure 14a–d).

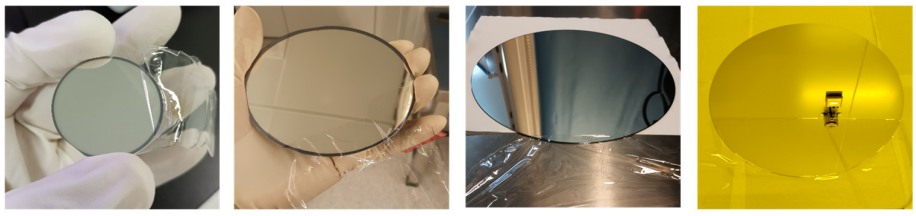

(a) (b) (c) (d)

Figure 14. Macroscopic demonstration of the peelable cleaning process on silver films with varying dimensions, illustrating the scalability and structural integrity of the PVA/additive film. (**a**–**d**) Optical photographs showing the intact peeling of the polymer film from silver substrates with diameters ranging from approximately 1 inch to 12 inches, confirming crack-free removal and surface preservation across large areas.

Taken together, the optical constant analysis, macroscopic morphology observations, and large-area sample validation confirm that the proposed peelable polymer cleaning strategy not only enables efficient removal of surface particulate contaminants, but also effectively preserves the structural integrity, surface continuity, and intrinsic optical func-

tionality of silver films throughout the cleaning process. This approach therefore provides a reliable and scalable pathway for the high-quality fabrication and practical application of precision metal thin-film systems.

To fully realize this scalable potential in industrial settings, future adaptations can seamlessly transition from the current manual peeling to automated processing. Specifically, the manual step can be effectively replaced by tension-controlled motorized rollers. By providing a consistent and operator-independent peeling force, such automated handling would further minimize human-induced stress variations, ultimately paving the way for continuous roll-to-roll, large-scale manufacturing of high-quality thin films.

4. Conclusions

In summary, this work presents a non-destructive cleaning strategy for silver films based on regulated polymer mechanical properties. By incorporating a carbonyl-containing hydrogen-bond-accepting polymer additive into poly(vinyl alcohol) (PVA), a tunable hydrogen-bonded network is constructed, enabling controlled modulation of polymer bulk cohesion and interfacial adhesion to silver films. This design confines fracture to the polymer/silver interface during mechanical peeling, allowing efficient removal of particulate contaminants without damaging the fragile silver layer. The optimized system achieves particle removal efficiencies of up to 98% for contaminants larger than 30 nm, while preserving film thickness, surface morphology, and intrinsic optical properties, and is applicable to silver films with lateral dimensions from 1 to 12 inches. By adjusting polymer curing parameters and additive composition, the cleaning strategy can be readily adapted to silver films of different thicknesses and mechanical responses. Compared with conventional chemical or physical cleaning approaches, this method offers a dry, residue-free, and stress-controllable solution, and provides a scalable route for the high-quality cleaning of other vulnerable metal thin films with potential benefits for advanced optoelectronic and nanophotonic devices.

Author Contributions: Conceptualization, Y.Z., T.S. and L.L.; methodology, Y.Z.; software, X.G.; validation, Y.Z., Y.D. and T.S.; formal analysis, Y.Z.; investigation, Y.Z., T.S., K.L., Y.L., C.Z. and Z.Z.; resources, Y.L., K.L., C.W. and L.L.; data curation, Y.Z.; writing—original draft preparation, Y.Z.; writing—review and editing, Y.D., T.S. and L.L.; visualization, Y.Z.; supervision, L.L.; project administration, L.L. All authors have read and agreed to the published version of the manuscript.

Funding: This research received no external funding.

Data Availability Statement: The original contributions presented in this study are included in the article. Further inquiries can be directed to the corresponding author.

Conflicts of Interest: The authors declare no conflicts of interest.

References

1. Zhang, C.; Ji, C.; Park, Y.B.; Guo, L.J. Thin-Metal-Film-Based Transparent Conductors: Material Preparation, Optical Design, and Device Applications. *Adv. Opt. Mater.* **2021**, *9*, 2001298. [CrossRef]
2. Kim, T.H.; Park, S.H.; Kim, D.H.; Nah, Y.C.; Kim, H.K. Roll-to-roll sputtered ITO/Ag/ITO multilayers for highly transparent and flexible electrochromic applications. *Sol. Energy Mater. Sol. Cells* **2017**, *160*, 203–210. [CrossRef]
3. Li, S.; Yu, T.; Du, C.; Deng, H.; He, X.; Zhao, Y.; Feng, Y.; Zhang, L.; Wang, Y.; Wang, D. Large-scale and ultra-thin conductive two-dimensional metal films (<3.5 nm) for fast flexible electronics. *Mater. Today* **2025**, *86*, 52–62. [CrossRef]
4. Wang, R.J.; Peng, J.Y.; Wang, S.; Bai, J.L.; Zhang, H.Z.; Yu, R.M.; Ji, W.Y. Optimizing Ag films towards efficient flexible quantum-dot light-emitting diodes. *Chem. Eng. J.* **2024**, *488*, 151313. [CrossRef]
5. Kinner, L.; Dimopoulos, T.; Ligorio, G.; List-Kratochvil, E.J.W.; Hermerschmidt, F. High-performance organic light-emitting diodes employing ITO-free and flexible TiO_x/Ag/Al:ZnO electrodes. *RSC Adv.* **2021**, *11*, 17324–17331. [CrossRef]
6. Song, C.; Feng, Y.; Bao, Z.Y.; Liu, G.L.; Wang, J.C. Angle-insensitive color filters based on multilayer ultrathin-film structures. *Plasmonics* **2020**, *15*, 255–261. [CrossRef]

7. Gao, Q.; Ao, J.P.; Bi, J.L.; Yao, L.Y.; Zhang, Z.J.; Zhang, Y.H.; Guo, J.J.; Sun, G.Z.; Zhang, Y.; Liu, W.; et al. A novel metal precursor structure for electrodepositing ultrathin CIGSe thin-film solar cells with high efficiency. *ACS Appl. Mater. Interfaces* **2020**, *12*, 24403–24410. [CrossRef] [PubMed]
8. Li, Z.J.; Li, H.J.; Chen, L.J.; Huang, J.H.; Wang, W.Y.; Wang, H.Q.; Li, J.; Fan, B.; Xu, Q.; Song, W.J. Semitransparent perovskite solar cells with ultrathin silver electrodes for tandem solar cells. *Sol. Energy* **2020**, *206*, 294–300. [CrossRef]
9. Zhang, X.R.; Yan, R.Y.; Guo, Z.M.; Li, P.; Feng, S.L. Quasimetal nanosize Te enhanced PbS nanorod photodetector with localized surface plasmon resonance effect. *Physica E* **2023**, *153*, 114397. [CrossRef]
10. Zhang, W.D.; Li, C.; Gao, K.; Lu, F.F.; Liu, M.; Li, X.; Zhang, L.; Mao, D.; Gao, F.; Huang, L.G.; et al. Surface-enhanced Raman spectroscopy with Au nanoparticle substrates fabricated using femtosecond laser pulses. *Nanotechnology* **2018**, *29*, 205301. [CrossRef]
11. Nagai, M. Impact of particulate contaminants on current leakage defects in OLED devices. *J. Electrochem. Soc.* **2007**, *154*, J387–J392. [CrossRef]
12. Le, Q.-T.; Guevenc, H.; Ibrahim, A.; Klipp, A.; Decoster, S.; Murdoch, G.; Sanchez, E.A. Wet cleaning of molybdenum for nano-interconnects. *ECS Trans.* **2022**, *108*, 39–46. [CrossRef]
13. Danel, A.; Raccurt, O. Understanding of wet and alternative particle removal processes in microelectronics: Theoretical capabilities and limitations. *J. Telecommun. Inf. Technol.* **2005**, *1*, 11–19. [CrossRef]
14. An, K.H.; Yerriboina, N.P.; Poddar, M.K.; Kim, T.G.; Lee, D.K.; Jung, T.H.; Lee, J.H.; Lee, H.H.; Park, J.G. Hybrid DHF and N_2 jet spray cleaning for silicon nitride and metal layer DRAM patterns. *Microelectron. Eng.* **2020**, *220*, 111148. [CrossRef]
15. Han, Z.; Keswani, M.; Raghavan, S. Megasonic cleaning of blanket and patterned samples in carbonated ammonia solutions for enhanced particle removal and reduced feature damage. *IEEE Trans. Semicond. Manuf.* **2013**, *26*, 400–405. [CrossRef]
16. Zhang, S.; Wang, F.; Tan, B.; Li, W.; Gao, B.; He, Y. Recent advances and future developments in PVA brush scrubbing cleaning: A review. *Mater. Sci. Semicond. Process.* **2022**, *152*, 107122. [CrossRef]
17. Wostyn, K.L.; Wada, M.; Andreas, M.; Kenis, K.; Roussel, P.; Bearda, T.; Leunissen, P.; Mertens, P. Particle removal and damage thresholds in high-velocity aerosol cleaning. *ECS Trans.* **2009**, *25*, 211–218. [CrossRef]
18. Walker, T.W.; Hsu, T.T.; Fitzgibbon, S.; Frank, C.W.; Mui, D.S.L.; Zhu, J.; Mendiratta, A.; Fuller, G.G. Enhanced particle removal using viscoelastic fluids. *J. Rheol.* **2014**, *58*, 63–88. [CrossRef]
19. Lin, P.; Pi, S.; Jiang, H.; Xia, Q. Mold cleaning with polydimethylsiloxane for nanoimprint lithography. *Nanotechnology* **2013**, *24*, 325301. [CrossRef]
20. Lallart, A.; Garnier, P.; Lorenceau, E.; Cartellier, A.; Charlaix, E. Cleaning surfaces from nanoparticles with polymer films: Impact of polymer stripping. *Micro Nano Eng.* **2018**, *1*, 33–36. [CrossRef]
21. Bergström, L. Hamaker constants of inorganic materials. *Adv. Colloid Interface Sci.* **1997**, *70*, 125–169. [CrossRef]
22. Israelachvili, J.N. *Intermolecular and Surface Forces*; Academic Press: San Diego, CA, USA, 2011.
23. Wang, Z.; Chu, Y.; Zhao, G.; Yin, Z.; Kuang, T.; Yan, F.; Zhang, L.; Zhang, L. Study of surface wettability of mineral rock particles by an improved Washburn method. *ACS Omega* **2023**, *8*, 15721–15729. [CrossRef]
24. Li, W.; Wang, L. The thermal stability of silver-based high reflectance coatings. *Thin Solid Film.* **2016**, *616*, 122–125.
25. Zhang, S.; Wei, D.; Xu, X. Transparent, high-strength, and antimicrobial polyvinyl alcohol/boric acid/poly(hexamethylene guanidine hydrochloride) films. *Coatings* **2023**, *13*, 1115. [CrossRef]
26. Pinchuk, A.O. Size-dependent Hamaker constant for silver nanoparticles. *J. Phys. Chem. C* **2012**, *116*, 20099–20102. [CrossRef]
27. Baburin, A.S.; Merzlikin, A.M.; Baryshev, A.V.; Ryzhikov, I.A.; Panfilov, Y.V.; Rodionov, I.A. Silver-based plasmonics: Golden material platform and application challenges. *Opt. Mater. Express* **2019**, *9*, 611–642. [CrossRef]